ACS APPLIED MATERIALS & INTERFACES

RESEARCH ARTICLE

www.acsami.org

Strain-Induce Shift of the Crystal-Field Splitting of $SrTiO_3$ Embedded in Scandate Multilayers

D. Ávila-Brande,*[,†,§] M. Boese,[†,∥] L. Houben,[†] J. Schubert,[‡] and M. Luysberg[†]

[†]Ernst Ruska-Centre and Institut für Festkörperforschung, Forschungszentrum Jülich, 52425 Jülich, Germany

[‡]Institut für Bio- und Nanosysteme, Forschungszentrum Jülich, 52425 Jülich, Germany

ABSTRACT: Strained $SrTiO_3$ layers have become of interest, since the paraelectric-to-ferroelectric transition temperature can be increased to room temperature. A linear relationship between strain and energy splitting of the fundamental transitions in the fine structure of Ti $L_{2,3}$ and O K edges is observed, that can be exploited to measure strain from electronic transitions, complementary to measuring local strain directly via high-resolution transmission electron microscopy (HRTEM) images. In particular, for both methods, the geometrical phase analysis performed on high-resolution images and the measurement of the energy splitting by energy loss spectroscopy, tensile strain of $SrTiO_3$ layers was measured when grown on $DyScO_3$ and $GdScO_3$ substrates. The effect of strain on the electron loss near edge structure (ELNES) of the Ti $L_{2,3}$ edge in comparison to unstrained samples is analyzed. Ab initio calculations of the Ti $L_{2,3}$ and O K edge show a linear variation of the crystal field splitting with strain. Calculated and experimental values of the crystal field splitting show a very good agreement

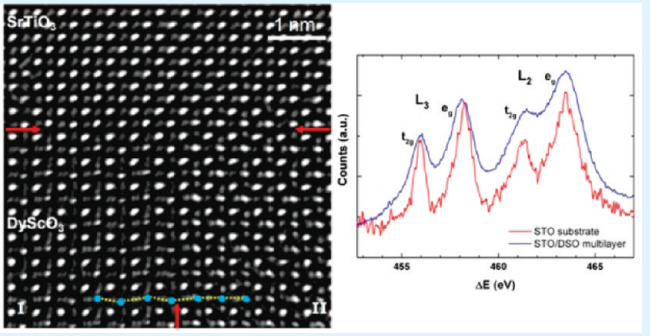

KEYWORDS: scandate/titanate multilayers, electron microscopy, strain, crystal field, ab initio calculations

1. INTRODUCTION

Thin films with a ferroelectric to paraelectric transition near room temperature are the object of an intense development for their use in different devices such as gate dielectrics for metal semiconductor field-effect transistors (MOSFETs).[1] $SrTiO_3$ (STO) is an incipient ferroelectric material but in its pure form at room temperature it exhibits a cubic structure and only at very low temperature dielectric properties are observed.[2] However, the Tc can be adjusted by chemical substitution as it has been previously observed in $Ba_xSr_{1-x}TiO_3$.[3] The main disadvantage of this methodology is the chemical heterogeneity within the film, resulting in a broadening of the phase transition temperature.

An alternative to tune the Tc of STO in thin films is the application of stress by the epitaxial growth on substrates with different lattice parameters or thermal expansion behavior.[4−8] In this sense, rare earth scandates ($REScO_3$ RE:La−Ho) are promising candidates because of the large range of available lattice constants depending on the rare earth cation inserted in the perovskite framework. Most of them crystallize in the orthorhombic $GdFeO_3$ type structure[9] in the space group *Pnma*, with lattice parameters $a \approx a_p\sqrt{2}$, $b \approx 2a_p$, and $c \approx a_p\sqrt{2}$, where a_p denotes the perovskite cubic lattice constant. The pseudocubic lattice parameter a_p can vary between 0.394 and 0.405 nm depending on the rare earth element, for example a_p ($DyScO_3$) = 0.395 nm and a_p ($GdScO_3$) = 0.397 nm. Therefore taking into account the cubic lattice constant of 0.3905 nm for $SrTiO_3$ a tensile strain is expected on its epitaxial growth onto rare earth scandates, resulting in ferroelectricity at room temperature. Since the strain has a strong influence on the dielectric properties, the quantitative determination of its value is crucial to understand how this methodology can be improved in the design of new materials with enhanced dielectric properties.

As mentioned above, strain produces a tetragonal distortion of the material which is traduced in a displacement of the atoms inside the strained material yielding a distorted unit cell with lower symmetry. These displacements, depending on the type of strain (compressive or tensile), affects the atomic bonds and therefore the electronic structure.

High resolution X-ray diffraction can be used to determine the new unit cell under strain, which will deliver a mean value for the volume investigated, i.e. about 1 mm^3. However in the case of multilayer systems it is also desirable to get information on the nanometer scale at the interfaces. Here, high resolution transmission electron microscopy (HRTEM) plays an important role because atomic resolution down to 0.8 Å can be achieved in the modern Cs-corrected transmission electron microscopes. On the other hand, Electron energy-loss spectroscopy (EELS) coupled with a Cs-probe corrected scanning transmission electron microscope (STEM) is a powerful analytical tool to probe the electronic band structure at atomic level in interfaces, nanoparticles, grain boundaries, etc.[10−12]

In this paper Cs-corrected microscopes in TEM and STEM modes are employed to investigate the atomic features of thin films within $SrTiO_3/DyScO_3$ (STO/DSO) and $SrTiO_3$/

Received: January 27, 2011
Accepted: April 4, 2011
Published: April 05, 2011

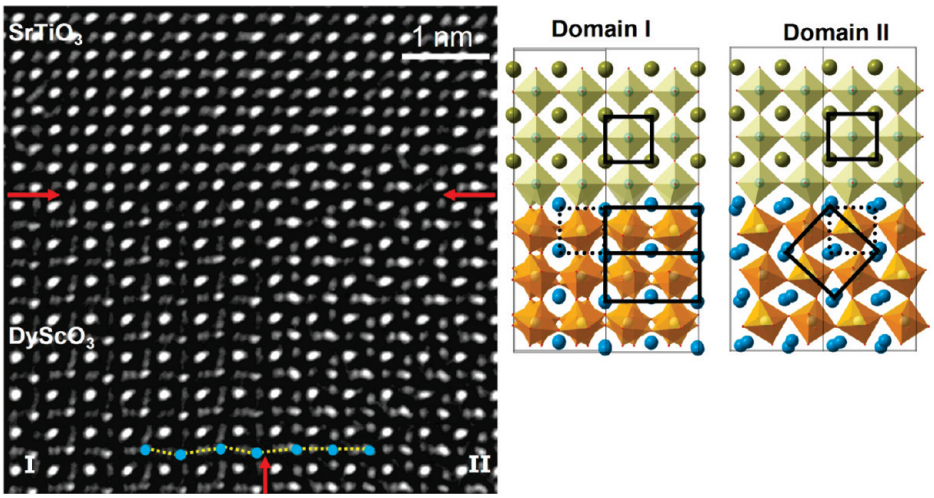

Figure 1. Experimental HRTEM of a STO/DSO multilayer. The image was taken under negative spherical aberration imaging conditions along the [001] zone axis, where, the cation as well as the oxygen atomic columns appear as bright dots. The schematics show projected views of the atomic structures corresponding to the domains I ([101] zone axis) and II ([010] zone axis). The grain boundary between domain I (left-hand side) and II (right-hand side) as well as the interface are indicated by red arrows.

$GdScO_3$ (STO/GSO) multilayers. In particular, the strain within the STO layers is measured by HRTEM and EELS. Ab initio calculations of the Ti L_3 edge reveal that the crystal field splitting of the Ti L_3 edge depends linearly on the strain. Hence, the crystal field splitting provides a measure of the strain in STO.

2. EXPERIMENTAL SECTION

Multilayers of $SrTiO_3/DyScO_3$ and $SrTiO_3/GdScO_3$ were deposited on $REScO_3$ (RE: Gd, Dy) (110) substrates. The multilayer system was grown by pulsed laser deposition (PLD) at a substrate temperature of 650−700 °C.[13] Cross-sectional samples for TEM investigation were obtained by mechanical grinding, polishing and dimpling down to a thickness of 20 μm followed by Ar ion milling (Baltec Res101). Initially an Ar energy of 5 kV was employed. Clean surfaces were achieved by a final treatment with 1 kV Argon ions.

Aberration-corrected high-resolution transmission electron microscopy was carried out in a FEI Titan 80−300 kV equipped with a CEOS double hexapole corrector having an information limit better than 0.08 nm at 300 kV. The so-called negative Cs imaging (NCSI) technique[14] provides bright atom contrast, at 300 kV when a negative spherical aberration value (Cs) of −13 μm and an optimum defocus (Z) setting of Z = +12 nm are established. In addition, focus series were acquired, some of them with a Cs corrected Philips CM200 microscope at Cs of −35 μm and Z = +8 nm and a resolution limit of just below 0.14 nm. The exit-plane wave was reconstructed using the "True Image" software (FEI), which is based on the Philips-Brite-Euram software package.[15,16]

EEL spectra were recorded in a probe aberration-corrected FEI Titan 80−300 microscope in STEM mode at 300 kV, equipped with a Wien-type electron monochromator and a Gatan GIF Tridiem 866 ERS post column energy filter. The probe semiconvergence and the effective collection angle was 25 mrad. The titanium L_3 and oxygen K-edges were calculated by means of real-space multiple scattering calculations, using the self-consistent version of this method implemented in the ab initio FEFF8.20 code.[17]

3. RESULTS AND DISCUSSION

3.1. Microstructure and Crystallographic Orientation Relationships. This paragraph briefly summarizes the crystallographic structure of the multilayer samples, in particular the orientation relationship between the cubic strontium titanate and the orthorhombic scandate layers. Figure 1 displays a typical high-resolution micrograph of a $SrTiO_3/DyScO_3$ interface. This image was obtained under NCSI conditions. Minor residual aberrations are still present, which can be deduced form the elongated shape of the Sr and Ti atom columns within the STO seen in the upper half of the image. Bright peaks are located at the atom positions. The intensity variation of each atom column with specimen thickness depends on the extinction coefficient. For the imaging conditions in Figure 1 no contrast difference of the Sr and Ti positions is observed, which agrees with image calculations.[18] In addition to the Sr and Ti signals, weak contrasts arising from the oxygen columns are clearly resolved. Because of the residual aberrations and/or a crystal tilt the position of the oxygen columns slightly deviates from the central position. The different oxygen sub lattices enable a clear identification of the different crystallographic domains. Within the $DyScO_3$ layer, two domains can be distinguished, which imply a 90° rotation with respect to each other. Domain I seen on the left-hand side is viewed along the [101] zone axis of $DyScO_3$ where the Dy atoms showing a weaker intensity than the Sc atoms are aligned in zigzag fashion parallel to the [001] direction, i.e. from left to right (see the yellow dotted line). The schematics displayed in Figure 1 show the atomic structure, where one unit cell is indicated by the solid rectangle. In addition, the pseudocubic unit cell of the $DyScO_3$ is highlighted by the dotted square. According to the tilted octahedra surrounding the Sc atoms within the DSO structure, two oxygen columns are located between the Dy columns in domain I. This is also clearly visible within the experimental image. On the right-hand side domain II prevails within the DSO layer, which is viewed along the [010] direction. Here, the Dy columns are aligned in a straight line parallel to the interface with one oxygen column located between the Dy columns. The domain boundary is marked by a red arrow. Both domains form a well-defined, sharp interface with the $SrTiO_3$ layer. Except for one location (of about 50) the long axis of the $DyScO_3$ or $GdScO_3$ unit cell is always observed to be perpendicular to the growth direction, which agrees with previous reports on orthorhombic perovskites.[18,19]

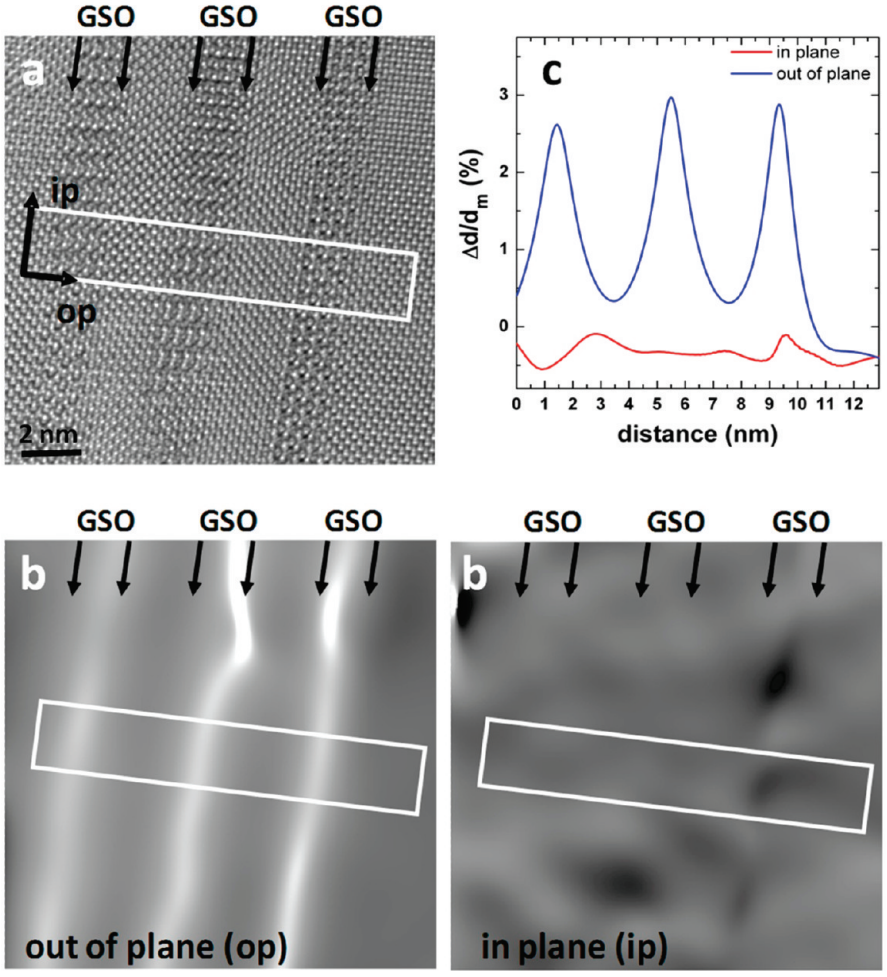

Figure 2. (a) NCSI image from a GSO/STO multilayer system used as input in the GPA analysis (interfaces are indicated by arrows). (b) Strain maps showing the lattice displacements of the "out of plane" (left-hand side) and "in plane" (right-hand side) components. **c**) Average line profiles evaluated along the white boxes in b.

3.2. Strain Quantification: Geometrical Phase Analysis (GPA). The geometrical phase analysis[20] is employed to measure the local tetragonal distortion of the strontium titanate layers. As input either NCSI images or reconstructed exit-plane wave functions are used. The method is based on the analysis of the spatial fluctuation of a frequency component in the Fast Fourier Transform (FFT) of an image[21] or a wave function in Fourier space. These fluctuations can be transformed into displacement maps that show deviations from the average lattice parameters. To measure the tetragonality, Fourier components corresponding to the out-of plane and in-plane lattice parameters are investigated, which correspond to the lattice parameters parallel and perpendicular to the growth direction respectively.

Figure 2 displays a GPA analysis for a GSO/STO multilayer system grown onto GSO substrate. The NCSI image is seen in Figure 2a, the corresponding displacement maps of the in-plane and out of plane components are shown in Figure 2b. The $(400)_{STO}$ and $(040)_{STO}$ reflections were chosen to evaluate the in-plane and out of-plane components, respectively. The contrast within these images scales linearly with the lattice parameter. The "in plane" image is characterized by small contrast fluctuations only. However the "out of plane" profile shows a drastic variation, where the bright contrasts indicating large lattice parameters coincide with the GSO layers. In the upper part of the out of-plane image artifacts occur, where the contrast is brightest. These contrasts can be caused by strong local variations of the lattice parameter, which arise from strain surrounding domain boundaries and different atom arrangement in the domains. Apart from these artifacts the strain is uniform, which can be deduced from the homogeneous contrast parallel to the layers. For further analyses regions of smooth contrast within the amplitude (not shown here) and phase images of both components are selected, such as the rectangular region superimposed to Figures 2a and b. From this region with a width of 2 nm line profiles perpendicular to the interfaces are evaluated, which are averaged parallel to the interface. Figure 2c displays the local deviation of the lattice parameter with respect to the mean lattice parameter of the out-of plane and in-plane image, respectively. The out of-plane component varies from −0.5% within the $SrTiO_3$ buffer layer (on the right-hand side of Figures2a and b) up to 3% within the first GSO layer at the right-hand side. The fact that the "in plane" component $\varepsilon_{||}$ shows hardly any variation indicates that the STO and GSO layers have the same in-plane lattice parameter in the area investigated. The variation of the in-plane lattice parameter is smaller than 0.5% or 2 pm, which is a measure of the precision of the measurement.

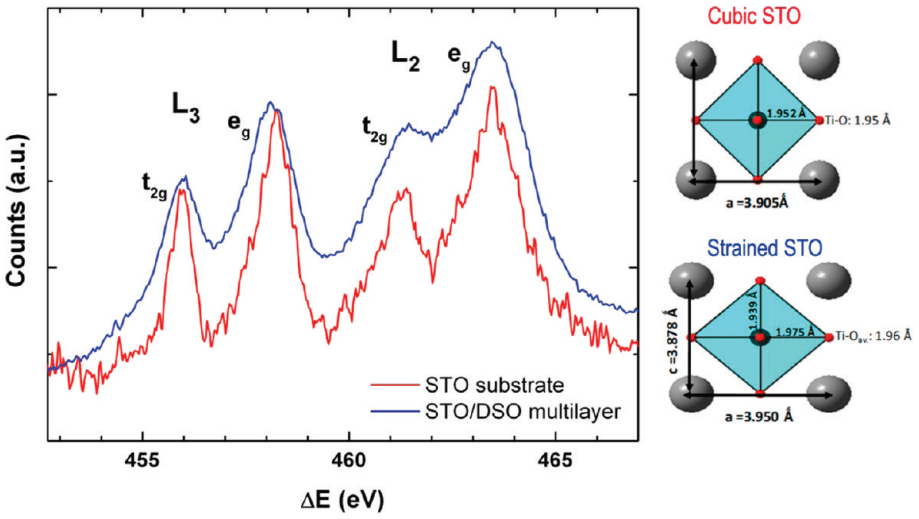

Figure 3. EEL spectra showing the Ti $L_{2,3}$ edges from unstrained and strained STO, which have been measured on a STO reference sample and STO grown onto DSO substrate. Clearly, the splitting of the L edges is reduced for the strained material. The schematic models on the right side display the effect of strain on the Ti−O bond lengths within the octahedron.

Since the multilayers were grown onto a GSO substrate, the in-plane lattice parameter of the STO buffer layer and of the STO multilayers can be assumed to be equal to that of GSO (a_{GSO}= 0.397 nm). From Figure 2c an average difference of the out-of-plane lattice parameters of 2.3% between STO and GSO is determined. The expected difference for unstrained STO and GSO is $(a_{GSO} - a_{STO})/[(a_{STO} + a_{GSO})/2]$ = 1.65% (The two values are significantly larger compared with the 0.5% maximum error of the measurement. Assuming that the GSO lattice remains unstrained, the out-of-plane lattice parameter $d_{STO}(OP)$ of the STO layers is calculated by $d_{STO}(OP) = (1-0.023) \times a_{GSO}$ = 388 pm. As a result a value of 0.6% = $(d_{STO}(OP) - a_{STO})/a_{STO}$ is obtained for the perpendicular strain $\varepsilon_{\perp}$, which is smaller than the theoretical value calculated by:

$$\varepsilon_{\perp} = \frac{2\nu}{1-\nu}\varepsilon_{\parallel} = \frac{2\nu}{1-\nu}\frac{a_{GSO} - a_{STO}}{a_{STO}} = 1\%$$

where the Poisson ratio ν = 0.23.[22] In view of the fact, that no misfit dislocation could be observed, it has to be concluded, that the STO layers are partially elastically relaxed. This elastic relaxation may occur due to the geometry of the TEM specimen, which implies a specimen thickness well below 20 nm in the area observed in Figure 2. Nonetheless, clear evidence for tensile strain within the $SrTiO_3$ layers is given.

In a similar way, tensile strain is detected, when a DSO/STO multilayer system is grown onto DSO substrate. Here a maximal distortion of 2% with respect to the average lattice parameter is measured which translates to 8 pm in distance yielding a compressive *c* parameter for the strained STO of 395 pm which is, of course smaller than its *a* lattice constant in the non strained cubic form. Hence, the growth of STO on DSO produces tensile strain in the cubic titanate, resulting in a new strained tetragonal cell with larger *a* and shorter *c* parameter with respect to the cubic STO.

3.3. Effect of Strain on the Electronic Structure: EELS and Ab Initio Calculations. EELS was employed to study the effect of the strain on the electronic structure in these materials. Figure 3 illustrates the experimental EEL spectra recorded in the multilayer system STO/DSO. The graph displays the features of the Ti $L_{2,3}$ edge of strained STO grown onto a DSO substrate in blue and from a cubic STO reference sample in red. The two measurements were recorded with an energy resolution of 0.3 and 0.6 eV, respectively. The Ti $L_{2,3}$ edge is formed by four well split peaks attributed to excitations of $2P_{3/2}$ and $2P_{1/2}$ subshells to unoccupied t_{2g} and e_g states.[23] In cubic STO, the Ti is surrounded by six oxygen atoms forming a regular octahedron with six equivalent Ti−O distances of 1.95 Å (see Figure 3). However under tensile strain this octahedron is distorted, with the four equatorial Ti−O distances larger than the two apical ones, yielding an average distance Ti−O of 1.96 Å

Table 1. Structural Parameters Used As Input in the Ab Initio Calculations of the Ti L_3 and O K Edges[a]

$\varepsilon_{\parallel}$ (%)	$\varepsilon_{\perp}$ (%)	space group	unit cell (nm)	coordinates (*x*, *y*, *z*)
−0.51	0.31	*P4/mmm*(121)	*a* = 0.3885	Sr (0, 0, 0)
				Ti (1/2, 1/2, 1/2)
			c = 0.3917	O (1/2, 0, 1/2)
				O (1/2, 1/2, 0)
0	0.00	*Pm*$\bar{3}$*m* (221)	*a* = 0.3905	Sr (0, 0, 0)
				Ti (1/2, 1/2, 1/2)
				O (0, 1/2, 1/2)
0.40	0.23	*P4/mmm*(121)	*a* = 0.3920	
			c = 0.3896	
1.15	0.69		*a* = 0.3950	Sr (0, 0, 0)
			c = 0.3878	Ti (1/2, 1/2, 1/2)
1.66	0.99		*a* = 0.3970	O (1/2, 0, 1/2)
			c = 0.3866	O (1/2, 1/2, 0)
2.43	1.45		*a* = 0.4000	
			c = 0.3848	

[a] The cell parameters for the tetragonal strained phase were calculated with the expression: $[(c_{STO} - c_x)/c_{STO}] = \varepsilon_{\perp} = [2\nu/(1-\nu)]\varepsilon_{\parallel} = [2\nu/(1-\nu)][(a_x - a_{STO})/a_{STO}]$ where a_x corresponds to the value of the substrate where STO is grown, that is, for GSO as substrate a_x= 0.3970 nm, c_x is the new parameter of the tetragonal strained cell obtained from the relationship between $\varepsilon_{\perp}$ and $\varepsilon_{\parallel}$ and ν =0.23.

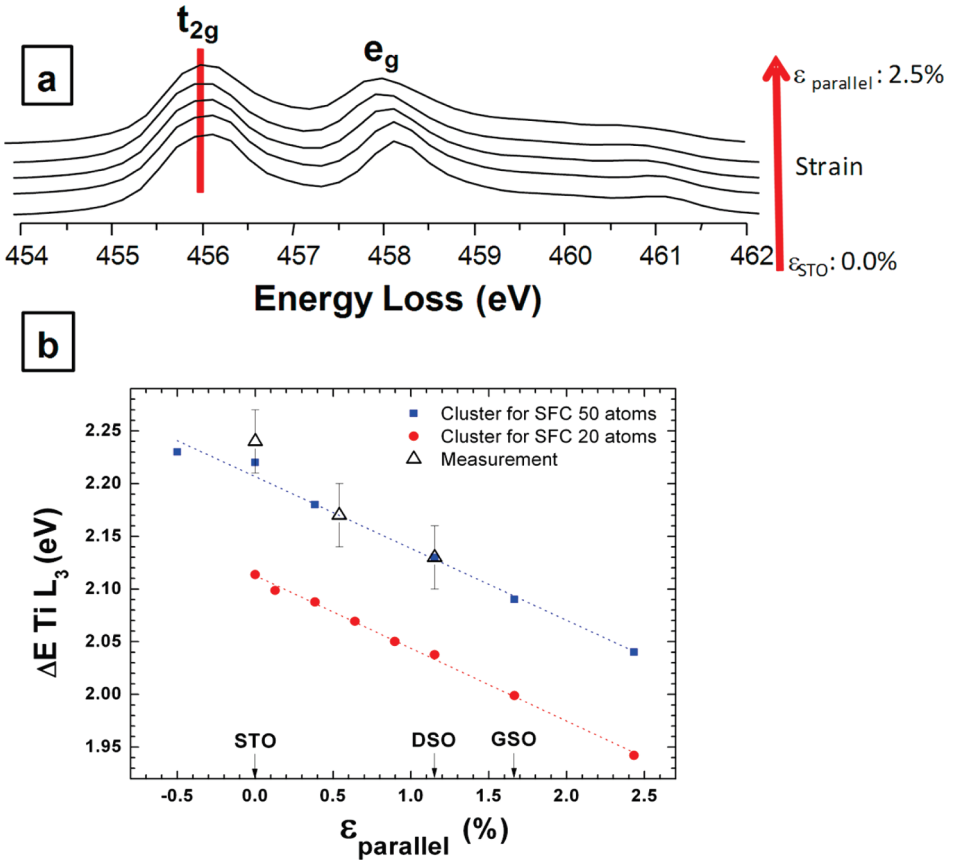

Figure 4. (a) Calculated Ti L_3 edges for different strain values for a cluster of 50 atoms. (b) The splitting of the L_3 edge calculated for different strain values (ε) and different cluster sizes (20 and 50 atoms) shows a linear decrease with increasing strain. Experimental values (triangles) show excellent agreement with calculations when the size of the cluster is 50 atoms.

(see Figure 3). This enlargement of the average bond length produces a weaker crystal field,[24] which is traduced in a smaller line splitting as it is observed in the blue spectrum. The splitting was measured by fitting Lorentzians to the peaks, which results in a precision of 0.02 eV. In addition, the dispersion was calibrated by assigning the first peak of the Sc L_{23} edge to 401 eV (not shown here) and of the Ti L_{23} edge to 456 eV. According to this procedure the total error in determination of the splitting is estimated to be smaller than 0.03 eV. The observation of a reduced crystal field splitting in strained STO is in line with the experimental data and ab initio calculations described by de Groot et al[25] in several d^0 compounds, where the splitting of the L lines has been calculated for different 10Dq values, that is, the crystal field parameter.

To evaluate the bonding effect, these situations were modeled by means of real-space full multiple scattering (FMS) calculations using the self-consistent version of this method implemented in the ab initio FEFF8.20 code.[26] The structural parameters for the cubic and tetragonal distorted $SrTiO_3$ used as input for the calculations are displayed in Table 1. The FEFF calculations were done with the Hedin−Lungqvist self-energies to account for inelastic losses and it is found that a cluster of about 50 atoms was sufficient to obtain well converged self-consistent field (SCF) potentials. For two cases, that is, a strain values of 0% and of 1.25%, calculations with larger clusters containing 150 atoms have been performed, which result in the same splitting of the Ti L_3 edge as obtained for a cluster of 50 atoms. For the FMS calculations, a cluster size of 185 atoms was used for both the titanium L_3 and oxygen K edges. The presence of final-state effects in the observed edges resulting from the core-level excitation is also taken into account. The core-hole effect is considered in the present FMS calculations with a fully relaxed potential in the presence of a core hole. The theoretical spectra were broadened by the experimental energy resolution, obtained by measuring the FWHM of the zero loss peaks.

Figure 4a represents the calculated titanium L_3 edges for different strain situations ranging from pure STO, where $\varepsilon_{\|} = 0$, to a large strain value of $\varepsilon_{\|}$ =2.5%. The larger the biaxial strain represented by $\varepsilon_{\|}$ the smaller is the splitting of the L_3 edge. These theoretical results are not surprising because the strain produces a distortion of the oxygen coordination around titanium, yielding under tensile strain four larger Ti−O distances and two shorter which correspond to the apical oxygen atoms perpendicular to the plane of strain. In average the distance Ti−O is always larger when increasing the value of $\varepsilon_{\|}$ but the most important finding is that the energy splitting of the L_3 edge decreases linearly when increasing the strain (see Figure 4b). As it is displayed in Figure 4b a cluster of only 20 atoms (circles) used in SCF calculations already reproduces the linearity. However, only for cluster sizes larger than 50 atoms the theoretical shift converges yielding an almost perfect agreement of calculated experimental (triangles) values. Two of the data points were measured from the spectra shown in Figure 3, where EEL spectra have been recorded within unstrained STO substrate and STO grown onto a DSO substrate.

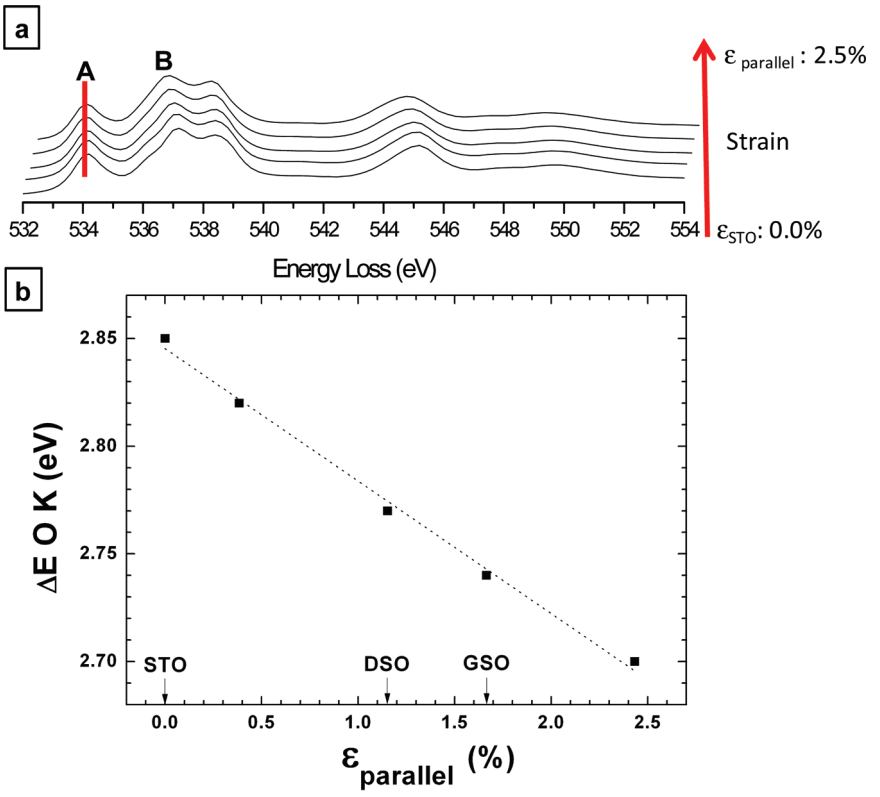

Figure 5. (a) Calculated O K edges for different strain values for a cluster of 50 atoms. (b).The separation of the first two peaks A and B of the O K edge shows a linear decrease with increasing strain.

The data agree very well with the splitting expected for a strain of 0% and 1.15%, respectively. If the measurement within the same STO/DSO sample is performed in a thin specimen area, a splitting of 2.17 eV is measured, which translates into a strain value of 0.54% according to the linear behavior shown in Figure.4b. This means, that the STO layer is not fully strained, which is in agreement with the strain measurements by the GPA (see Chapter 3.2), where elastic relaxation within the thin areas of the sample was detected as well. Since multiplet effects are ignored by FMS calculations, the intensity of the peaks is not correct because the peak t_{2g} is overestimated,[27] which however is not of relevance for the determination of peak positions.

The ELNES of the O K edge gives also information about different coordination around the oxygen atom. It has been described that the first two peaks of the oxygen K edge are related to the hybridization of the titanium 3d orbitals with the oxygen 2p and their separation is related to the crystal field splitting.[28] Therefore the calculated oxygen K edges should provide similar information as in the previously described case of Ti L edges. Figure 5a shows the calculated spectra for the same strain situations used before. Again, increasing the strain results in a smaller separation between the two first peaks, called A and B, i.e. a linear behavior is revealed in Figure 5b.

It is well-known, that the Ti atom within a strained oxygen octahedron can be shifted with respect to central position, which causes ferroelectrical behavior of $SrTiO_3$.[7] Hence, it is expected, that the Ti atoms within the biaxially strained STO layers investigated here, may not be located at the central position of the octahedra. However, such a shift of the Ti atom is not likely to affect the splitting of the fundamental transitions in the Ti L edges and O K edge, because the average bond length is maintained. Indeed, ab initio calculations of such asymmetric octahedra (not shown here), did not reveal any change in the crystal field splitting.

So far only biaxially dilatations of $SrTiO_3$ have been discussed, which match the experimental situation in scandate/STO multilayer systems. It is worth noticing, that also for compressive strain the linear relationship of crystal field splitting and strain is maintained, which can be deduced from the data point at a strain of −0.5% included into Figure 4. Hence, it is expected, that the crystal field splitting is a measure of biaxial compressive strain as well.

4. CONCLUSIONS

In this work, structure and strain within scandate/titanate multilayers have been investigated by high resolution transmission electron microscopy and electron energy loss spectroscopy. It was theoretically found that the tetragonal distortion induced by tensile strain results in a smaller splitting of the Ti L_3 and the first two peaks of the O K edge according to the lower crystal field. A linear decrease of the splitting occurs with increasing strain, offering a simple means to measure strain in thin strontium titanate layers. The experimental measurements of the Ti L_3 edge splitting for strontium titanate under tensile strain show an excellent agreement with the theoretical calculations. In contrast to the well established geometrical phase analysis, which uses high-resolution images as input data, the measurement of the splitting of the peaks in the ELNES can be performed on thick sample areas, where elastic relaxation can be omitted. Hence, the "true" strain of the bulk samples is obtained from measurements of the crystal field splitting.

AUTHOR INFORMATION

Corresponding Author

*Telephone: +34-91394-5161. Fax: +34-91394-4352. E-mail: avilad@quim.ucm.es.

Present Addresses

[§]Departamento de Química Inorgánica I, Fac. CC. Químicas, Universidad Complutense, 28040 Madrid.

[∥]Centre for Research on Adaptive Nanostructures and Nanodevices, Trinity College Dublin, Dublin 2, Ireland.

ACKNOWLEDGMENT

D.A. acknowledges the Fundación Ramón Areces for the concession of a postdoctoral grant.

REFERENCES

(1) Schlom, D. G.; Haeni, J. H. *Mater. Res. Soc. Bull.* **2002**, *27*, 198–204.

(2) Müller, K. A.; Burkard, H. *Phys. Rev. B* **1979**, *19*, 3593–3602.

(3) Canedy, C. L.; Li, H.; Alpay, S. P.; Salamanca-Riba, L.; Roytburd, A. L.; Ramesh, R. *Appl. Phys. Lett.* **2000**, *77*, 1695–1697.

(4) Devonshire, A. F. *Philos. Mag. Suppl.* **1954**, *3*, 85–130.

(5) Uwe, H.; Sakudo, T. *Phys. Rev. B* **1976**, *13*, 271–286.

(6) Abe, K.; Yanase, N.; Sano, K.; Izuha, M.; Fukushima, N.; Kawakubo, T. *Integr. Ferroelectr.* **1998**, *21*, 197–206.

(7) Haeni, J. H.; Irvin, P.; Chang, W.; Uecker, R.; Reiche, P.; Li, Y. L.; Choudhury, S.; Tian, W.; Hawley, M. E.; Craigo, B.; Tagantsev, A. K.; Pan, X. Q.; Streiffer, S. K.; Chen, L. Q.; Kirchoefer, S. W.; Levy, J.; Schlom, D. G. *Nature* **2004**, *430*, 758–761.

(8) Choi, K. J.; Biegalski, M.; Li, Y. L.; Sharan, A.; Schubert, J.; Uecker, R.; Reiche, P.; Chen, Y. B.; Pan, X. Q.; Gopalan, V.; Chen, L.-Q.; Schlom, D. G.; Eom, C. B. *Science* **2004**, *306*, 1005–1009.

(9) Geller, S. *J. Chem. Phys.* **1956**, *24*, 1236–1239.

(10) Grogger, W.; Hofer, F.; Kraus, B.; Rom, I.; Sitte, W.; Warbichler, P. *Mikrochim. Acta* **2000**, *133*, 125–129.

(11) Kim, M.; Duscher, G.; Browning, N. D.; Sohlberg, K.; Pantelides., S. T.; Pennycook, S. J. *Phys. Rev. Lett.* **2001**, *86*, 4056–4059.

(12) Zhang, Z.; Sigle, W.; Rühle, M. *Phys. Rev. B* **2002**, *66*, 094108/1–8.

(13) Heeg, T.; Wagner, M.; Schubert, J.; Buchal, C. H.; Boese, M.; Luysberg, M.; Cicerrella, E.; Freeouf, J. L. *Microelectron. Eng.* **2005**, *80*, 150–153.

(14) Haider, M.; Uhleman, S.; Schwan, E.; Rose, H.; Kabius, B.; Urban, K. *Nature* **1998**, *392*, 768–769.

(15) Coene, W. M. J.; Thust, A.; Op De Beeck, M.; Van Dyck, D. *Ultramicroscopy* **1996**, *64*, 109–135.

(16) Thust, A.; Coene, W. M. J.; Op De Beeck, M.; Van Dyck, D. *Ultramicroscopy* **1996**, *64*, 211–230.

(17) Ankudinov, A. L.; Bouldin, C. E.; Rehr, J. J.; Sims, J.; Hung, H. *Phys. Rev. B* **2002**, *65*, 104107/1–11.

(18) Boese, M.; Heeg, T.; Schubert, J.; Luysberg, M. *J. Mater. Sci.* **2006**, *41*, 4434–4439.

(19) Ma, X. L.; Zhu, Y. L.; Meng, X. M.; Lu, H. B.; Chen, F.; Chen, Z. H.; Yang, G. Z.; Zhang, Z. *Philos. Mag. A* **2002**, *82*, 1331–1343.

(20) Hytch, M.; Snoeck, E.; Kilaas, R. *Ultramicroscopy* **1998**, *74*, 131–146.

(21) Hüe, F.; Hÿtch, M.; Bender, H.; Houdellier, F.; Claverie, A. *Phys. Rev. Lett.* **2008**, *100*, 156602/1–4.

(22) Tarsa, E. J.; Hachfeld, E. A.; Quinlan, F. T.; Speck, J. S.; Eddy, M. *Appl. Phys. Lett.* **1996**, *68*, 490–492.

(23) Leapman, R. D.; Grunes, L. A. *Phys. Rev. Lett.* **1980**, *45*, 397–401.

(24) Zhang, J.; Visinoiu, A.; Heyroth, F.; Syrowatka, F.; Alexe, M.; Hesse, D.; Leipner, H. S. *Phys. Rev. B* **2005**, *71*, 064108/1–12.

(25) de Groot, F. M. D.; Fuggle, J. C.; Thole, B. T.; Sawatzky, G. A. *Phys. Rev. B* **1990**, *41*, 928–937.

(26) Moreno, M. S.; Jorissen, K.; Rehr, J. J. *Micron* **2007**, *38*, 1–11.

(27) Zhang, J. Application of Electron Energy-Loss Spectroscopy to Ferroelectric Thin Films. PhD thesis, Halle, 2004.

(28) de Groot, F. M. F.; Grioni, M.; Fuggle, J. C.; Ghijsen, J.; Sawatzky, G. A.; Petersen, H. *Phys. Rev. B* **1989**, *40*, 5715–5723.